

# Efficient Adsorption of a Sulfonamide Antibiotic in Aqueous Solutions with N-doped Magnetic Biochar: Performance, Mechanism, and Reusability

Yuan Diao, Rui Shan, Mei Li, Jing Gu, Haoran Yuan,\* and Yong Chen

Cite This: *ACS Omega* 2023, 8, 879–892

Read Online

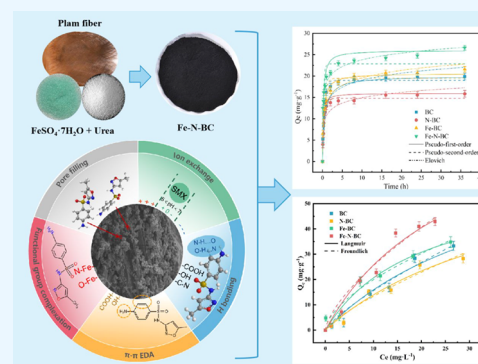
ACCESS |

Metrics &amp; More

Article Recommendations

Supporting Information

**ABSTRACT:** Conventional biochar has limited effectiveness in the adsorption of sulfonamide antibiotics, while modified biochar exhibits greater adsorption potential. Residues of sulfamethoxazole (SMX) in the aquatic environment can threaten the safety of microbial populations as well as humans. In this study, iron–nitrogen co-doped modified biochar (Fe-N-BC) was prepared from palm fibers and doped with Fe and urea via synthesis at 500 °C. Fe-N-BC has a richer surface functional group based on elemental content, X-ray photoelectron spectroscopy, X-ray diffraction, and Fourier transform infrared spectroscopy. The Brunauer–Emmett–Teller (BET) specific surface area test exhibited Fe-N-BC, which possessed a greater surface area (318.203 m<sup>2</sup>/g) and a better developed pore structure (0.149 cm<sup>3</sup>/g). The results of the hysteresis loop and the Raman spectrum show that Fe-N-BC has a higher degree of magnetization and graphitization. Fe-N-BC showed a remarkable adsorption capacity for SMX (42.9 mg/g), which could maintain 93.4% adsorption effect after four cycles, and 82.8% adsorption capacity in simulated piggy wastewater. The adsorption mechanism involves pore filling, surface complexation, electrostatic interactions, hydrogen bonding, and  $\pi$ – $\pi$  EDA interactions. The results of this study show that Fe-N-BC prepared from palm fibers can be a stable, excellent adsorbent for SMX removal from wastewater and has promise in terms of practical applications.



## 1. INTRODUCTION

Antibiotics such as cephalosporins, macrolides, sulfonamides, and quinolones are widely utilized in human medicine, livestock farming, and aquaculture.<sup>1,2</sup> Among these, sulfonamides are one of the most traditional classes of synthetic broad-spectrum antibacterial drugs; however, due to their extremely low bioavailability and long half-life in the environment,<sup>3</sup> sulfonamide antibiotics are constantly detected in the aqueous environment. Besides harming microorganisms, algae, and aquatic plants, the persistence of antibiotics in the environment increases the resistance of pathogenic bacteria, causing them to develop resistance genes,<sup>4</sup> which are transferred to animals and humans with drinking water and food, making antibiotic treatments fail and thus increasing the risk of human infection and death.<sup>5</sup> Therefore, it is necessary to explore efficient and economical technologies to remove sulfonamide antibiotics from contaminated water. There are methods to remove sulfonamide antibiotics individually or in combination with chemical, biodegradation, advanced oxidation, and physical and chemical methods.<sup>6–8</sup> The adsorption method is widely used in organic pollution treatment with its advantages of low cost, easy recovery, and no secondary pollution.<sup>9</sup> The selection and preparation of the adsorbent is the key to the successful application of the adsorption method.<sup>10</sup> As an economical and environmentally friendly

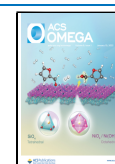
adsorption material, biochar attracts attention for its high removal efficiency, simple operation, and low production cost.<sup>11</sup>

Many research studies have reported that biochar can effectively adsorb various organic pollutants (antibiotic drugs,<sup>12</sup> dyes,<sup>13</sup> volatile organic compounds,<sup>14</sup> etc.). Nowadays, researchers are committed to applying various modification approaches to enrich the pore structure and enlarge the surface area of biochar,<sup>15</sup> for example, the functionalization of biochar, the magnetization method, and the surface oxidation method.<sup>11</sup> Although it has been demonstrated that the modified biochar can improve contaminant removal, it is challenging to separate biochar from the liquid by traditional precipitation and filtration processes, and the biochar is prone to mass loss during recycling. Recent research on modification methods has focused on the biochar magnetization technology, in which iron, cobalt, nickel, and their alloys were embedded with the

Received: September 27, 2022

Accepted: December 5, 2022

Published: December 22, 2022



biochar to modify the biochar,<sup>16</sup> which retained the traditional adsorption performance of the biochar and made it magnetic. After adsorption, solid-liquid separation and re-recovery are performed by external magnetic attraction.<sup>17</sup> Generally, iron imparts magnetism to biochar through chemical co-precipitation<sup>18</sup> or one-step method.<sup>19</sup> However, chemical co-precipitation has complex steps, where adsorption sites and pore structures are occupied on the surface of biochar. By contrast, magnetic biochar is mainly prepared using a one-step technique. On the other hand, the one-step method alone cannot provide enough functional groups for biochar surfaces, so further modification methods are considered.<sup>20</sup>

At present, there are various techniques to further modify biochar, including oxidation,<sup>15</sup> chemical treatment,<sup>21</sup> or other elements are added in the preparation process of the biochar to generate expected functional groups.<sup>22</sup> We have noticed that studies have pointed out that N doping of biochar plays a promoting role in removing heavy metals,<sup>23</sup> acid gases,<sup>24</sup> and organic contaminants.<sup>25</sup> Nitrogen doping can induce physical and chemical property changes in biochar. The introduction of nitrogen into the ordered sp<sup>2</sup> hybrid graphite layer of biochar can generate localized imbalanced charged regions and more active sites in the carbon structure due to the promotion of the polarization of  $\pi$  electrons.<sup>26</sup> In addition, the N atom doped on the surface of the biochar enhances electron mobility, improves the biochar's hydrophobic property, and increases the affinity for pollutants.<sup>22</sup> Therefore, the combination of iron and nitrogen co-modifications may be an excellent means to make the biochar possess magnetism while also increasing the surface functional groups.

Moreover, some researchers have applied the iron–nitrogen co-modified biochar to the advanced oxidation field or to adsorb heavy metals. Liu et al. found that the iron–nitrogen composite biochar could work together with sodium sulfide to rapidly break the azo bond of methyl orange and convert it into aromatic amine, thus realizing the rapid decolorization of methyl orange.<sup>27</sup> Ren et al. utilized NH<sub>3</sub> and FeSO<sub>4</sub> generated from Mohr's salt decomposition to conduct a carbothermal reaction with biochar to synthesize a ferrous sulfide-loaded nitrogen-doped biochar composite material. This material exhibited outstanding performance and stability while removing Cr(VI) from water.<sup>28</sup> Doping N on the aromatic carbon ring of biochar can generate positive holes, and the resulting difference in electronegativity can attract electron-rich organic contaminants because the molecular arrangement of the organic pollutants was more nucleophilic. Fe-N co-doped biochar could promote the adsorption of organic pollutants through  $\pi$ – $\pi$  EDA interactions and Lewis acid–base interactions.<sup>29</sup> Biochar can enhance the removal of contaminants through the surface rich in nitrogen-containing functional groups and highly dispersed and stable iron oxides. The use of N-doped magnetic biochar as an adsorbent for sulfonamides is rarely reported. Additionally, in earlier studies, most attention has been paid to the pore structure of biochar and its removal of pollutants. However, the regeneration performance of biochar and the mass loss during its recycling deserves further investigation.

To explore the adsorption and reuse capability of biochar for sulfonamide antibiotics, palm tree fibers were utilized in this work as the feedstock for the manufacture of biochar. Palm fiber is a kind of weblike palm-coated fiber created by the palm poles' peripheral leaf sheaths,<sup>30</sup> which are extensively used for rope production and mattress filling but have limited

applications.<sup>31</sup> The low-density porous structure of palm fiber drew our attention.<sup>32</sup> This study synthesized a novel Fe-N-BC biochar by palm fiber, urea, and FeSO<sub>4</sub>·7H<sub>2</sub>O. It was utilized to adsorb sulfamethoxazole (SMX), the most prevalent sulfonamide antibiotic species in water.<sup>33</sup> The effects of variables including initial pH value and coexisting ions on the reaction were investigated. In addition, different desorption methods were used to evaluate the impacts on Fe-N-BC reusability, and the practical usage of Fe-N-BC was investigated by mimicking the adsorption of sulfonamide antibiotics from piggery wastewater. Brunauer–Emmett–Teller (BET), X-ray photoelectron spectroscopy (XPS), X-ray diffraction (XRD), zeta potential, and other characterization techniques were used to examine the adsorption mechanism of the Fe-N-BC/SMX system.

## 2. MATERIALS AND METHODS

**2.1. Materials.** The palm fiber was collected from palm bark in Guangzhou, China. After being washed with deionized water until free of brown lint and dust, they were placed in an oven at 80 °C for 12 h, then crushed in a pulverizer. Urea, FeSO<sub>4</sub>·7H<sub>2</sub>O, glucose, NH<sub>4</sub>NO<sub>3</sub>, NH<sub>4</sub>Cl, NaH<sub>2</sub>PO<sub>4</sub>, CH<sub>4</sub>N<sub>2</sub>O, NaCl, CaCl<sub>2</sub>, NH<sub>4</sub>Cl, MgSO<sub>4</sub>, methanol, H<sub>2</sub>O<sub>2</sub>, SMX, KH<sub>2</sub>PO<sub>4</sub>, and MgSO<sub>4</sub>·7H<sub>2</sub>O were purchased from Aladdin Biochemical Co., Ltd. (Shanghai, China). All chemicals were of analytical pure, and deionized water was used in all experiments. SMX was dissolved with 0.01 mol/L NaOH and configured into a standard stock solution of 100 mg/L, which was stored at 2 °C, valid for three months.

**2.2. Biochar Characterization.** Thermogravimetric analysis was performed by a thermogravimetric analyzer (TG-DSC, NETZSCH STA 449, Germany) with a biomass weight of 10 mg at temperatures ranging from 50 to 900 °C in a N<sub>2</sub> atmosphere. Field emission scanning electron microscopy (SEM, HITACHI SU70, Japan) and transmission electron microscopy (TEM, JEOL JEM-2100F) were applied to characterize the morphology of the adsorbent surface. The elemental composition was clarified by an elemental analyzer (Vario EL cube, Germany). The specific surface area and pore structure were obtained by a BET analyzer (BET, Micromeritics ASAP2460, USA) in the N<sub>2</sub> adsorption–desorption isotherm at 77 K. The vibrating sample magnetometer (VSM, Lake Shore 7404, USA) was used to analyze the magnetic properties of the samples. The zeta potential of biochars was evaluated by a zeta potentiometer (Zetasizer, Mastersizer 2000E, UK) in the pH range of 3.0–10.0. The functional group composition was analyzed by Fourier transform infrared (FTIR, Thermo Nicolet iN10) spectroscopy. The surface elements and chemical composition of the biochars were determined by XPS (Thermo ESCALAB 250XI, USA). The crystal structure of biochars was analyzed by XRD (Rigaku Corporation Smartlab, Japan) in the range of 25–65° $2\theta$  at a step size of 0.4°.

**2.3. Preparation of Biochar.** Fe-N-BC biochar was prepared by the processes below: In the first phase, the palm fiber powder was combined in a 1:1:3 mass ratio with urea and FeSO<sub>4</sub>·7H<sub>2</sub>O.<sup>3,4</sup> Deionized water (110 mL) was added to the mixture and put on a magnetic stirrer, then spun at 500 rpm for 24 h to fully permeate the raw material with two modified substances, and then dried in a 75 °C oven for 12 h. In the second phase, the dried solid was placed in a tube furnace with N<sub>2</sub> protection and heated to 500 °C at a speed of 5 °C/min for 2 h. In the third step, the biochar was washed with deionized

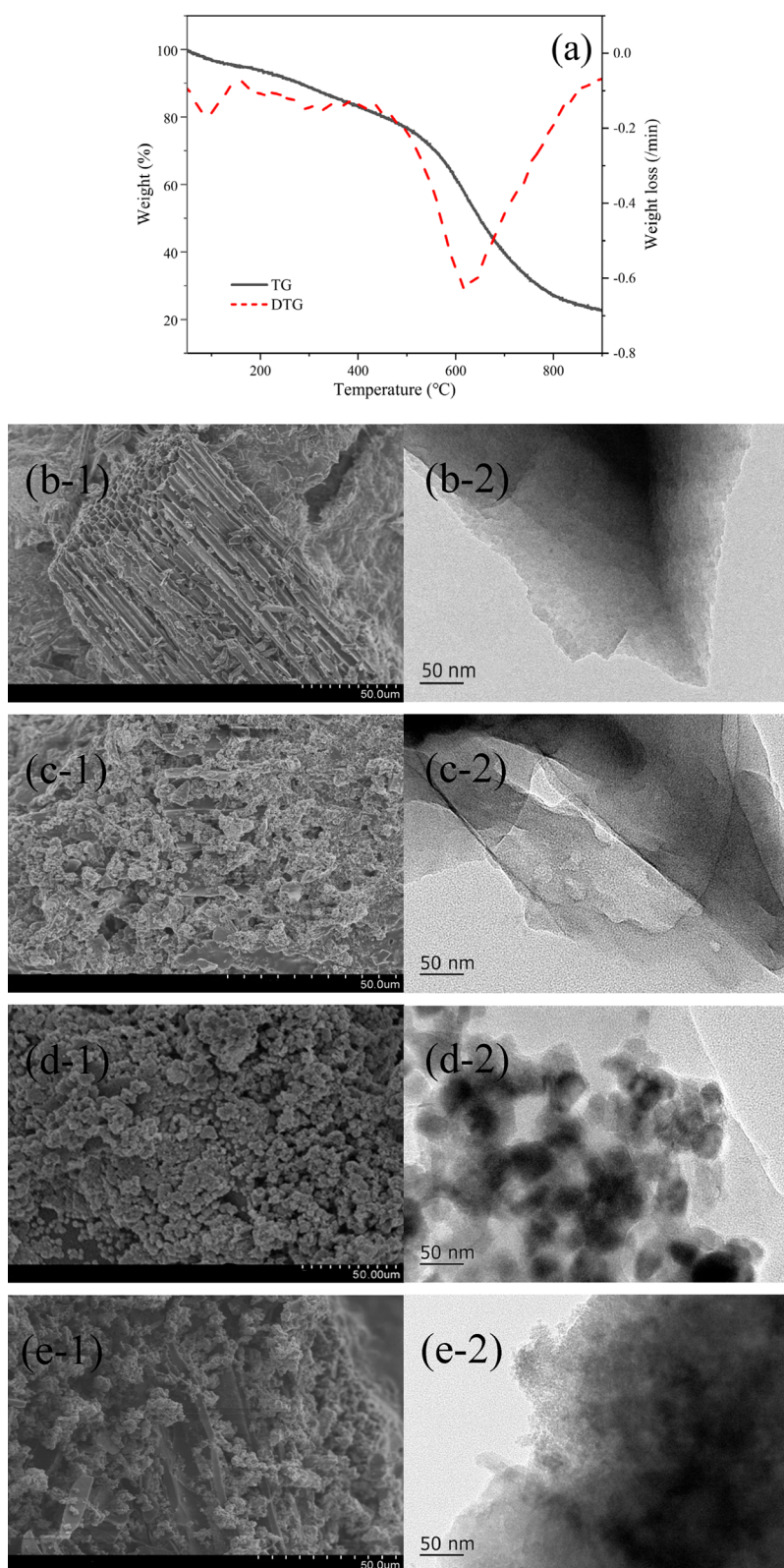


**Figure 1.** (a) TGA of palm fiber at 10 °C/min; SEM images of (b-1) BC, (c-1) N-BC, (d-1) Fe-BC, and (e-1) Fe-N-BC; TEM images of (b-2) BC, (c-2) N-BC, (d-2) Fe-BC, and (e-2) Fe-N-BC.

water to neutrality and dried at 60 °C, after which it was ground into a 150 mesh powder. Meanwhile, BC (palm fiber), Fe-BC (palm fiber,  $\text{FeSO}_4 \cdot 7\text{H}_2\text{O}$ ), and N-BC (palm fiber, urea) were used as controls and were pyrolyzed and treated in the same way as Fe-N-BC.

**2.4. Adsorption Experiment.** The sulfonamide antibiotics in solution were determined by high-performance liquid chromatography (HPLC) (Agilent 1200) at 270 nm, and the separation was carried out by the C18 column (diameter, length, and pore size = 2.1 mm, 150 mm, and 3.5  $\mu\text{m}$ ). The

mobile phase was 0.1% formic acid (solvent A)/acetonitrile (solvent B) = 80/20 (V/V), and separation was performed at a column temperature of 35 °C while the injection volume was 5  $\mu$ L at a flow rate of 1 mL/min. The system's retention time was 3 min, and it took 5 min to equilibrate before the next injection.

The batch adsorption experiments were carried out in 150 mL conical flasks with 50 mL of SMX solution at different initial concentrations, and different types of biochar were added at a solid–liquid ratio of 0.5 g/L. The pH of the solution was adjusted to  $5 \pm 0.1$  with 0.01 mol/L HCl and 0.01 mol/L NaOH, then placed the solution on a shaker and shaken at 180 r/min for 12 h. Then, the solution was centrifuged, and the supernatant was taken with a disposable syringe and filtered by a 0.45  $\mu$ m filter head for SMX concentration detection. In order to evaluate the impact of pH, the buffered solution was employed to adjust the pH of the solution within the range of 3 to 10. Four ions ( $\text{Na}^+$ ,  $\text{Ca}^{2+}$ ,  $\text{NH}_4^+$ , and  $\text{Mg}^{2+}$ ) were selected as co-existing ions in the solution,<sup>35</sup> while the concentrations were diluted to 0.01, 0.05, 0.1, and 0.2 mol/L. All the experiments were repeated three times for each group, with the average and standard deviation recorded.

**2.5. Adsorption–Regeneration Experiments.** Two different desorption solutions were selected to desorb the SMX on the spent biochar to investigate the reusability of biochar.<sup>29</sup> Group A was  $\text{H}_2\text{O}_2$  and methanol (MeOH) (0.1:10 mol/L,  $V = 1:1$ ), and group B was ammonia and methanol (1:20 mol/L,  $V = 1:1$ ). The spent biochar and regeneration solution were added to the conical flask at a ratio of 1:10 ( $w/V$ ). After shaking for 24 h to desorb the SMX from the biochar, it was filtered, dried, and subjected to subsequent adsorption experiments. The cycle was performed four times.

**2.6. Data Analysis.** The removal efficiency eq 1 and adsorption capacity eq 2 of SMX were calculated with the following formula:

$$Q_t = \frac{(C_0 - C_t) V}{m} \quad (1)$$

$$Q_e = \frac{(C_0 - C_e) V}{m} \quad (2)$$

where  $Q_e$  (mg/g) and  $Q_t$  (mg/g) represent the adsorption amounts of SMX at equilibrium and at time  $t$ ;  $C_0$  (mg/L) and  $C_e$  (mg/L) are the initial concentration and the equilibrium concentration of SMX, respectively.

The four classical models for fitting experimental data in kinetics were the pseudo-first-order eq 3, Elovich model eq 4, pseudo-second-order eq 5, and intraparticle diffusion eq 6.

$$Q_t = Q_e(1 - e^{-k_1 t}) \quad (3)$$

$$Q_t = \ln(\alpha\beta)/\beta + \ln t/\beta \quad (4)$$

$$Q_t = \frac{k_2 Q_e^2}{1 + k_2 Q_e t} \quad (5)$$

$$Q_t = k_i' t^{0.5} + C_i \quad (6)$$

where,  $k_1$  ( $\text{min}^{-1}$ ),  $k_2$  ( $\text{g}/(\text{mg}\cdot\text{min})$ ),  $\alpha$  ( $\text{mg}/(\text{g}\cdot\text{min})$ ),  $\beta$  ( $\text{g}/\text{mg}$ ), and  $k_i'$  ( $\text{mg}/(\text{g}\cdot\text{min}^{0.5})$ ) are rate constants for different kinetics;  $C_i$  describes the boundary layer properties.

The concentrations of SMX were set at 0, 2, 15, 20, 30, and 40 mg/L, respectively. Experimental data of isotherms were fitted by two models, Freundlich eq 7 and Langmuir eq 8, which are written as follows:

$$Q_e = K_F C_e^{1/n} \quad (7)$$

$$Q_e = \frac{Q_0 K_L C_e}{1 + K_L C_e} \quad (8)$$

where  $K_L$  and  $K_F$  represent the constants of the Langmuir isotherm and the Freundlich isotherm;  $n$  is the empirical parameter of the Freundlich isotherm.

The mass loss, the cumulative mass loss rate eq 9, and the retained adsorption efficiency eq 10 of biochar were calculated in four cycles of regeneration experiments.

$$L_n = \frac{\sum_{i=0}^n l_n}{1000} \times 100\% \quad (n = 1, 2, 3, 4) \quad (9)$$

$$R = \frac{Q_e'}{Q_e} \times 100\% \quad (10)$$

where  $l_n$  (mg/g) and  $Q_e'$  (mg/g) are the mass loss of biochar and the adsorption capacity of biochar for SMX in the  $n$ th cycle test, respectively.

**2.7. Adsorption Experiments in Synthetic Piggery Wastewater.** The impact of Fe-N-BC in the adsorption of sulfonamide antibiotics in synthetic piggery wastewater was investigated. According to the characteristics of high organic matter concentration and ammonia nitrogen concentration of piggery wastewater,<sup>36</sup> the main components of synthetic wastewater were designed as glucose,  $\text{NH}_4\text{NO}_3$ ,  $\text{NH}_4\text{Cl}$ ,  $\text{NaH}_2\text{PO}_4$ ,  $\text{CH}_4\text{N}_2\text{O}$ ,  $\text{KH}_2\text{PO}_4$ ,  $\text{MgSO}_4 \cdot 7\text{H}_2\text{O}$ , and  $\text{CaCl}_2 \cdot 2\text{H}_2\text{O}$  with the concentrations of 2840 mg/L, 400, 450, 200, 100, 132, 50, and 10 mg/L, respectively. The stock solution of sulfonamide antibiotics was configured with the synthetic wastewater at a concentration of 15 mg/L, and the same dose of the adsorbent (0.5 g/L) was used. Adsorption was performed for 24 h at 25 °C and 150 rpm, and the initial pH of solution was not adjusted.

### 3. RESULTS AND DISCUSSION

**3.1. Characterization of Biochar.** The thermogravimetric analysis (TGA) of the palm fiber pyrolysis process is shown in Figure 1a. The mass of palm fiber slowly decreased as the temperature increased from 100 to 500 °C due to the breakdown of cellulose and hemicellulose, losing about 79.5% of its weight. When the temperature was raised to 800 °C, the mass decreased to about 20% due to the disintegration of lignin in the feedstock.<sup>37</sup> Therefore, biochar BC and Fe-N modified biochar were chosen to be manufactured at 500 °C to ensure biochar yield in this study.

The SEM and TEM images presented the surface morphology and pore structure of the four biochars. It can be observed that the undoped palm fiber (Figure 1b) has a cross-section that resembles a tightly packed honeycomb, and the thicker char layer has an uneven and amorphous surface. The rough surface and pore structure serve as an excellent foundation for further loading and adsorption. After N modification, the surface remained amorphous and adhesive agglomeration of palm fiber fragments was observed (Figure 1c), which is attributed to the condensation reaction between urea and palm fiber, preventing the pore structure develop-

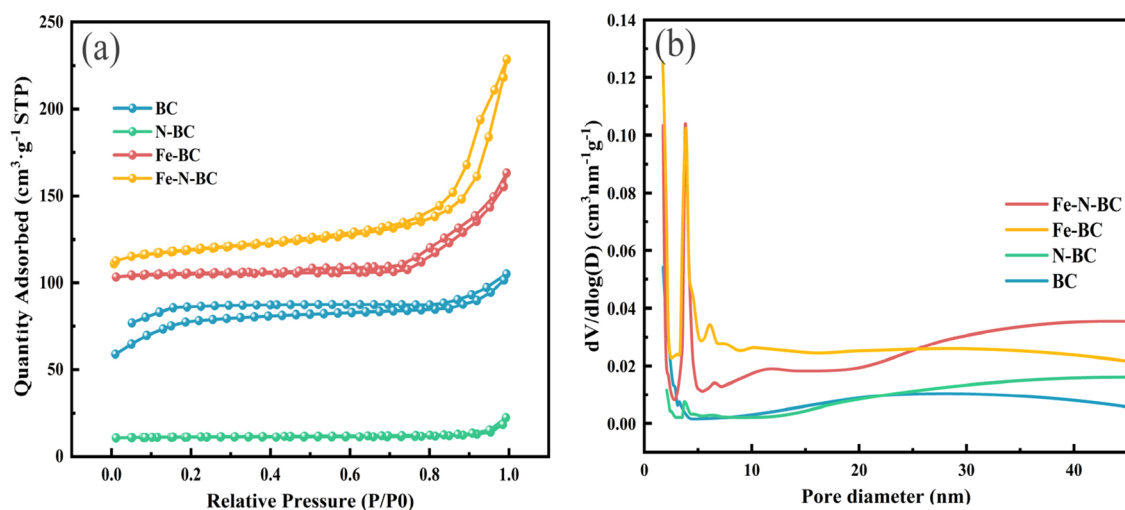


Figure 2. (a) BET isotherms and (b) pore size distribution curves.

Table 1. Surface Structure Characteristics of Different Palm Fiber Biochars

biochar	BET surface area (m <sup>2</sup> /g)	micropore area (m <sup>2</sup> /g)	total pore volume (cm <sup>3</sup> /g)	micropore volume (cm <sup>3</sup> /g)	micro/total pore volume (%)	average pore size (nm)
BC	287.614	189.797	0.136	0.076	0.56	1.890
N-BC	74.307	62.461	0.078	0.010	0.12	7.268
Fe-BC	288.063	150.640	0.161	0.079	0.49	2.475
Fe-N-BC	318.203	213.250	0.149	0.105	0.51	1.473

Table 2. Elemental Composition of the Biochars

	C (%)	H (%)	N (%)	O (%)	H/C	O/C	(O + N)/C
BC	82.23	3.20	0.45	10.72	0.04	0.42	0.42
N-BC	73.56	2.93	9.86	9.85	0.04	0.35	0.48
Fe-BC	18.70	0.93	0.27	25.69	0.05	0.53	0.54
Fe-N-BC	31.95	1.67	5.08	34.31	0.05	1.07	1.23

ment. The thinning of the biochar carbon layer following iron doping, the large number of spherical particles shown in the SEM image, and the dark spots shown in the TEM image (Figure 1d), which can be linked to the formation of iron oxide. Therefore, the pore structure of the biochar became obvious. After doping with Fe and N, irregular nanoparticles were discovered on the surface of biochar (Figure 1e), further generating the pore structure.<sup>38</sup> The dark dots distributed in the carbon structure in the TEM images indicate that the iron oxide nanoparticles are highly dispersed. The pyrolyzed biochar was finer than palm fiber biochar, with rougher surfaces, more voids, and a more regular carbon structure with less overlap. These characteristics may be able to add more active sites and increase the reaction area for the adsorption process.

The type of adsorption isotherms in N<sub>2</sub> is an important index to evaluate the performance of the adsorbent. The adsorption isotherm curves of the three modified biochars displayed in Figure 2a, which can be categorized as Type IV isotherms with H3-type hysteresis loops according to the IUPAC classification,<sup>39</sup> indicate that the adsorption of the biochars is mesopore adsorbent and has capillary condensation of multilayer adsorption. According to the pore size distribution curves (Figure 2b), the pore sizes of the four biochars were concentrated between 2 and 4 nm, confirming that the pores in the samples were mainly mesopores. Meanwhile, the BET experiments yielded the pore volume

and specific surface area of biochars. The BET specific surface area (288.063 m<sup>2</sup>/g) and total pore volume ( $V_{\text{total}}$ ) (0.161 cm<sup>3</sup>/g) of the Fe-BC biochar increased when Fe had alone been added, as shown in Table 1, because the presence of Fe reduced the shrinkage of carbon during the thermal decomposition of biochar.<sup>40</sup> Compared to BC, when Fe and N were co-doped, the BET specific surface area (318.203 m<sup>2</sup>/g), micropore area ( $S_{\text{micro}}$ ) (213.250 m<sup>2</sup>/g), and  $V_{\text{total}}$  (0.149 cm<sup>3</sup>/g) of Fe-N-BC were significantly increased. These data indicate that due to the presence of urea, Fe doping formed more micropores and mesopores on palm fibers, acting as a pore aid, which was consistent with SEM observations. In contrast, after nitrogen doping alone, the BET specific surface area (74.307 m<sup>2</sup>/g),  $S_{\text{micro}}$  (62.461 m<sup>2</sup>/g), and  $V_{\text{total}}$  (0.078 cm<sup>3</sup>/g) of N-BC significantly decreased, along with an increase in the average pore size to 3.8 times that of BC (7.268 cm<sup>3</sup>/g). These changes were attributed to the significant amount of gas produced by urea during pyrolysis, which caused the carbon framework to break down and produced a large number of pores.<sup>41</sup>

Based on the micro/total pore volume ( $V_{\text{m/t}}$ ) ratio of BC (0.56%), it can be seen that micropores and mesopores predominate. Compared to BC, Fe-N-BC (0.51%) had a lower  $V_{\text{m/t}}$  ratio, indicating that its surface mesopores were much more developed. Additionally, the  $V_{\text{m/t}}$  ratio of Fe-N-BC was higher than those of single nitrogen-doped biochar (N-BC, 0.12%) and single iron-doped biochar (Fe-BC, 0.49%). The

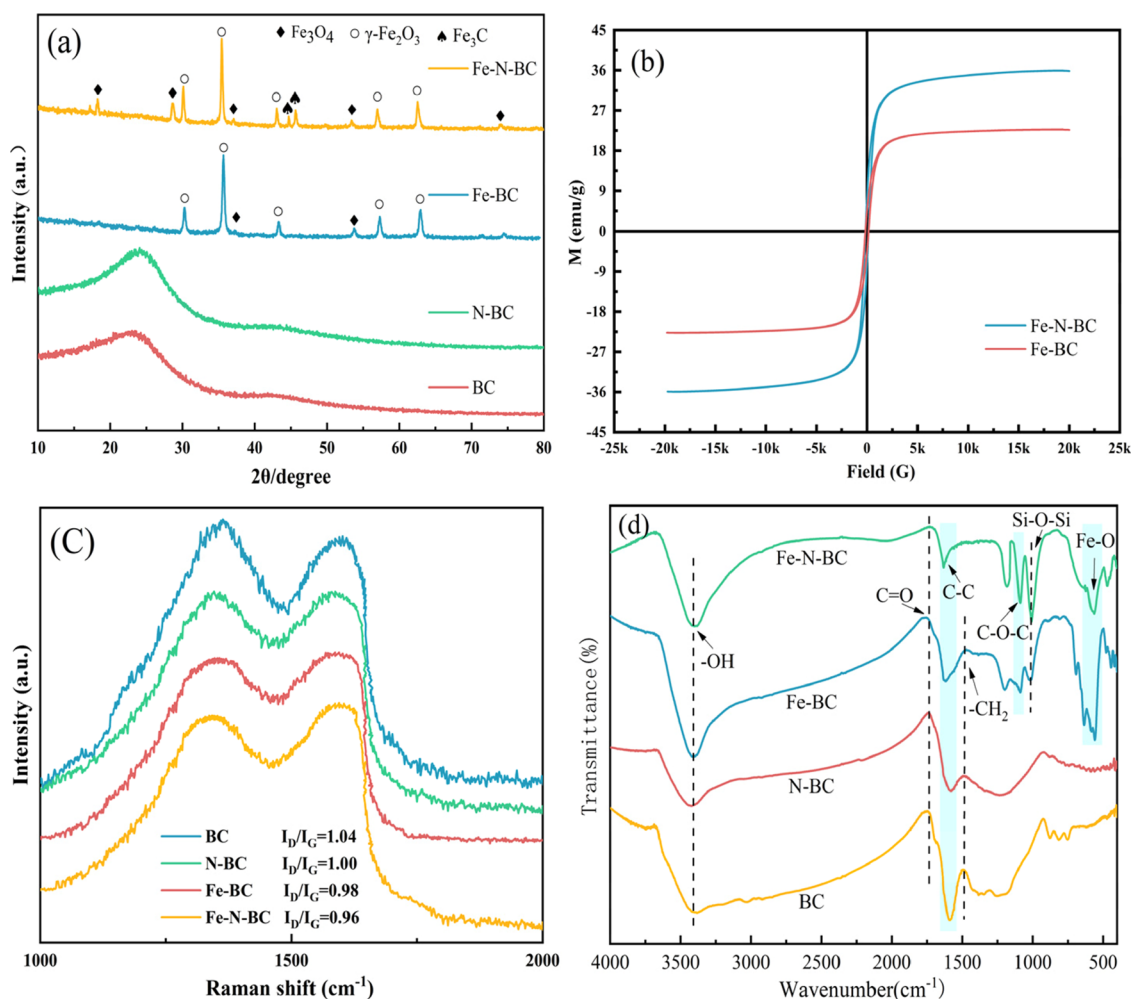


**Figure 3.** (a) XRD, (b) magnetic hysteresis loops, (c) Raman spectra of biochars, and (d) FTIR spectra of biochars.

results showed that the enrichment of pores of Fe-N-BC was accompanied by an increase in the specific surface area, providing additional attachment sites for its adsorption of SMX.

Elemental analysis (Table 2) revealed that with the doping of N and Fe, the C contents of N-BC, Fe-BC, and Fe-N-BC became lower. The proportion of C in Fe-BC and Fe-N-BC fell from 82.23% (BC) to 18.70 and 31.95%, respectively. The content of O rose after Fe modification, mainly due to the generation of iron oxide on the surface of biochar. Compared to BC, the proportion of N in N-BC and Fe-N-BC had risen from 0.45 to 9.85% and 5.08%, respectively, illustrating that prior impregnation had been successful in doping Fe and N into the biochar. The H/C ratio Fe-N-BC was slightly increased compared to other biochars, indicating a decline in the aromaticity<sup>42</sup> and a weakening of the  $\pi$ - $\pi$  EDA interaction between the biochars and the pollutants. Therefore, the adsorption mechanism of SMX on Fe-N-BC was likely to be altered. In addition, the O/C and (O + N)/C values of Fe-N-BC increased to 2.5 and 2.9 times those of BC, respectively. These findings showed that there are higher surface polarity and more oxygen-containing functional groups on Fe-N-BC.

The crystal structure of the biochar can be obtained from the XRD test results, as shown in Figure 3a. The original biochar BC diffraction peaks have two peaks, one at 23° formed by the amorphous carbon and the other at 42.35°

formed by the graphitic carbon structure. In the N-doped biochar (N-BC), the amorphous carbon peak is shifted to 24.37°, and the peak generated by the graphitic carbon structure tends to be flat. Because the Fe doping destroyed the carbon structure of the biochar, the intensity of the peaks generated by the amorphous char disappeared in the other two types of Fe doped biochar. Additionally, several characteristic peaks of Fe-containing substances were observed in the range of 20–80°.<sup>43</sup> Based on the above findings, Fe has been successfully loaded onto the biochar surface. These Fe oxides on the surface of the biochar could offer more active sites, which are favorable for the attachment of contaminants. The presence of  $\gamma$ -Fe<sub>2</sub>O<sub>3</sub>, Fe<sub>3</sub>O<sub>4</sub>, and Fe<sub>3</sub>C on the Fe-N-BC surface demonstrates that the coexistence of Fe and N did alter the carbon structure of biochar, and the reduction of Fe oxide was encouraged by the presence of nitrogen.

Figure 3b displays the hysteresis curves of Fe-BC and Fe-N-BC at room temperature (25 °C). The saturation magnetization strengths of the two types of Fe doped biochar were 22.04 (Fe-BC) and 35.81 (Fe-N-BC) emu/g, which were related to the formation of Fe<sub>3</sub>O<sub>4</sub> on the surface of the biochars. The saturation magnetization adsorption capacity of the biochar was improved by the addition of nitrogen.<sup>43</sup> It exhibited a slight coercivity with no significant magnetization hysteresis, indicating that both biochars have superparamagnetic properties.<sup>44</sup> The iron-containing biochar (Fe-BC and

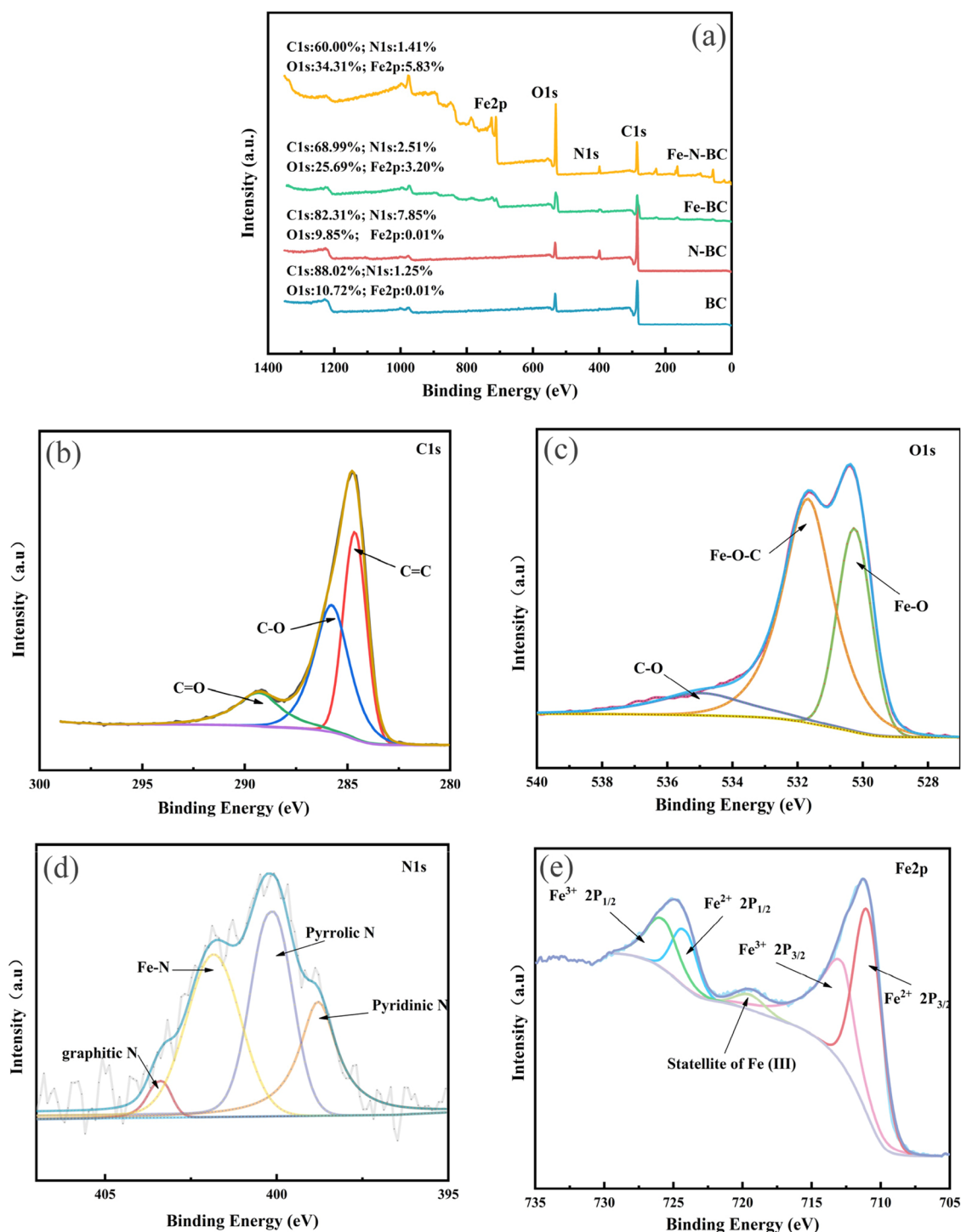


**Figure 4.** (a) XPS of biochars; (b) C 1s, (c) O 1s, (d) N 1s, and (e) Fe 2p XPS spectra of Fe-N-BC.

Fe-N-BC) can be easily separated from the solution by an applied magnetic field.

The crystallization and defects of the biochar were revealed using Raman spectroscopy, and Figure 3c displays the findings. The characteristic peak near 1360 cm corresponds to the peak D (disordered graphitic carbon), and near 1600 cm corresponds to G (sp<sup>2</sup>-hybridized graphitic carbon).<sup>45</sup> A measure of the degree of graphitization is the ratio of the D peak to the G peak's intensity ( $I_D/I_G$ ), and a higher ratio represents a larger carbon structural defect. The lower  $I_D/I_G$  values for N-BC (1.00) and Fe-BC (0.98) compared to pristine

biochar indicate that both modification methods result in a reduction of carbon defects in biochar, while the  $I_D/I_G$  ratio further decreases for Fe-N-BC (0.96), suggesting that the co-doping of Fe and N enhances the graphitization degree of biochars.

The characterization of the surface functional groups of the biochar can be characterized by FTIR spectroscopy. A control of the four biochars can be seen in Figure 3d. Similar peaks are present at 3420, 1740 cm<sup>-1</sup> and can be attributed to vibrations in the -OH and C=O bonds, respectively. For BC, N-BC, and Fe-BC the peaks near 1475 cm<sup>-1</sup> represent a vibration of

Table 3. Parameters of Kinetic Models for SMX Adsorption on the Four Biochars

		BC	N-BC	Fe-BC	Fe-N-BC
pseudo-first-order	$Q_e$ (mg/g)	$18.979 \pm 0.410$	$14.777 \pm 0.329$	$19.480 \pm 0.866$	$22.853 \pm 1.091$
	$k_1$ (/min)	2.293	2.520	2.053	4.181
	adj. $R^2$	0.976	0.975	0.901	0.843
pseudo-second-order	$Q_e$ (mg/g)	$15.963 \pm 0.174$	$20.061 \pm 0.325$	$20.602 \pm 0.560$	$26.533 \pm 0.207$
	$k_1$ (g/(mg·min))	0.458	0.081	0.152	0.186
	adj. $R^2$	0.826	0.712	0.970	0.910
Elovich	$\alpha$ (mg/(g·min))	0.867	0.820	0.770	1.905
	$\beta$ (g/mg)	0.423	0.549	0.396	0.440
	adj. $R^2$	0.923	0.917	0.979	0.987
intraparticle diffusion	$k_1$ (mg/(g·min <sup>0.5</sup> ))	2.142	1.900	1.553	1.293
	adj. $R^2$	0.978	0.968	0.906	0.941
	$k_2$ (mg/(g·min <sup>0.5</sup> ))	0.465	0.256	0.647	0.529
	adj. $R^2$	0.841	0.796	0.972	0.896
	$k_3$ (mg/(g·min <sup>0.5</sup> ))	0.039	0.060	0.083	0.109
	adj. $R^2$	0.913	0.871	0.908	0.927

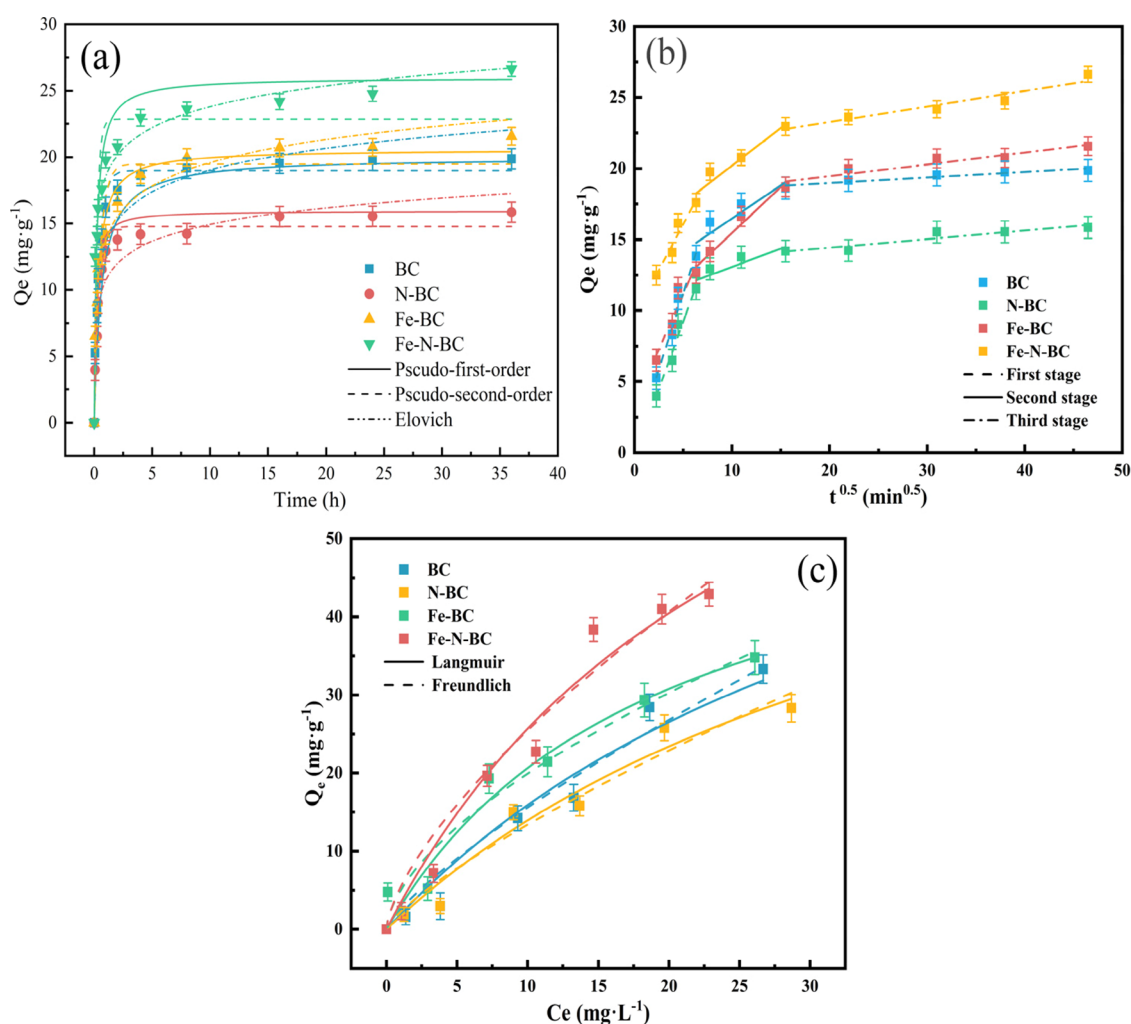


**Figure 5.** Adsorption kinetics of SMX fitted by (a) PFO, PSO, Elovich, and (b) intraparticle diffusion; (c) Langmuir and Freundlich isotherms for SMX on biochars.

–CH that diminishes with N loading and disappears in Fe-N-BC indicating that iron promotes the decomposition of organic matter in palm fibers.<sup>34</sup> Fe–O (568 cm<sup>-1</sup>) was found in the magnetized biochar, the intensity decreasing with N doping; the other peaks at 1020 and 1100 cm<sup>-1</sup> correspond to C–O–C and Si–O–Si bonds, both becoming stronger after N

doping. The peak intensity of the C–C or C=C bond at 1600 cm<sup>-1</sup> decreases progressively with Fe and N doping,<sup>28</sup> indicating that the aromatic structure is reduced but the alkanes and olefins are retained in the Fe–N modified biochar. The above results demonstrate that Fe and N intruded into the

Table 4. Fitting Parameters of the Adsorption Isotherm Models

	Langmuir			Freundlich		
	$Q_0$ (mg/g)	$K_L$ (L/mg)	adj. $R^2$	$K_F$	$n$	adj. $R^2$
BC	$33.310 \pm 0.328$	0.0248	0.955	2.570	0.7829	0.964
N-BC	$28.311 \pm 0.103$	0.0235	0.957	2.248	0.775	0.948
Fe-BC	$34.783 \pm 0.461$	0.0515	0.952	4.952	0.6045	0.962
Fe-N-BC	$42.903 \pm 0.227$	0.0234	0.966	5.380	0.8348	0.952

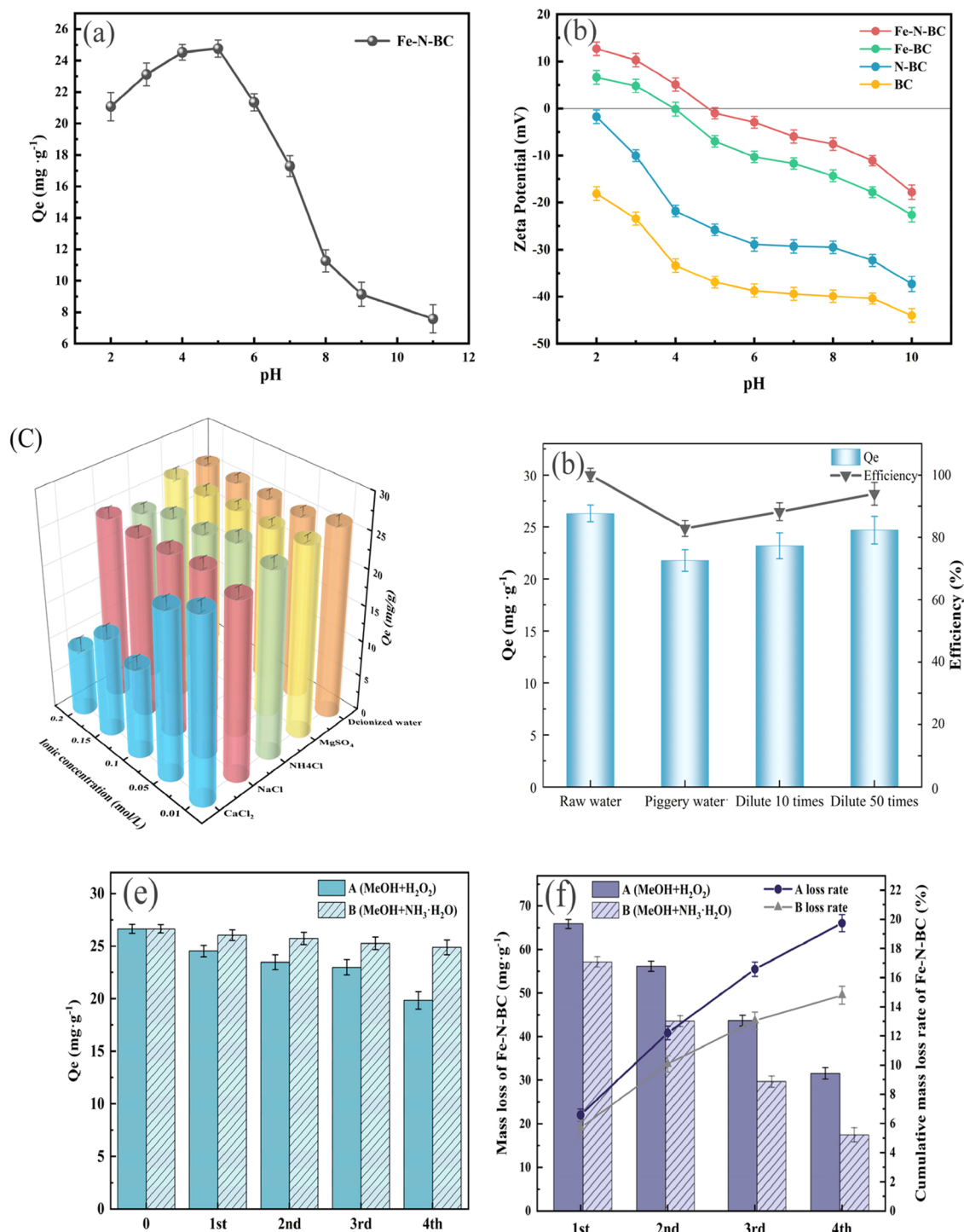


**Figure 6.** (a) Zeta potential of biochars; (b) adsorption capacity of Fe-N-BC for SMX at different pH levels; adsorption capacity of Fe-N-BC for SMX; (c) co-existence cation; (d) simulated piggery wastewater; four adsorption cycles of Fe-N-BC; (e) adsorption capacity; (f) mass loss.

carbon structure of biochar and can increase the number and type of functional groups on the surface of biochar.

The chemical composition of the surfaces of the four biochars was studied using XPS. As shown in Figure 4a, three peaks at 282.95, 397.97, and 530.03 eV, corresponding to C 1s, N 1s, and O 1s, respectively, were detected simultaneously in all biochar samples. In addition, Fe 2p (708.95 eV) photoelectron spectrum showed in both Fe-BC (Figure 4c) and Fe-N-BC (Figure s1c) X-ray photoelectron spectra. Compared with the pristine biochar (BC), the C content in the iron-modified biochars (Fe-BC and Fe-N-BC) fell to 68.99 and 60.00%, respectively; after modifying with N, the N content in N-BC increased significantly to 7.85%. The Fe-BC modified with Fe alone contained 3.20% Fe; after the Fe and N co-introduction, the contents of Fe and N in Fe-N-BC were 5.83 and 1.41%, respectively, demonstrating that the carbon matrix has been successfully doped with iron and nitrogen.

The C1s spectrum of Fe-N-BC has three main types of peaks (Figure 4b) at 284.23, 285.82, and 288.39 eV, corresponding to C=C/C-C (62.05%), C-OH/C-N (17.38%) and C-O-C (21.03%), respectively. The C 1s spectrum of BC (Figure s1a) can be divided into three peaks, C=O (22.29%), C=C (63.24%), and C-H (14.47%), indicating that Fe-N modified the morphology of the carbon structure. The corresponding O 1s spectrum of Fe-N-BC is shown in Figure 4d, with 530.22, 531.69, and 534.48 eV corresponding to Fe-O, C-OH, and C-O, respectively, with Fe-O bonds appearing after the Fe-N modification.<sup>34</sup> The fitted results of the N 1s spectra of Fe-N-BC correspond to 398.78, 400.07, 401.88, and 403.29 eV for pyridine N (21.30%), pyrrole N (36.11%), Fe-N (34.26%) and graphite N (8.33%) in four sub-peaks. After the nitrogen modification, N replaces a C on the hexagonal C structure in the graphitic carbon plane, forming a C-N bond, producing pyridine N, confirming nitrogen was doped in the nitrogen-modified carbon structure.<sup>36</sup> The presence of the Fe<sup>2+</sup> compound is confirmed by the peaks in the Fe-N-BC Fe 2p spectrum at 711.05 and 724.23 eV, while satellite peaks at 712.83 and 726.36 are assigned to the Fe<sup>3+</sup> compound. These Fe-compound were verified by XRD spectra results and identified as Fe<sub>2</sub>O<sub>3</sub> and Fe<sub>3</sub>O<sub>4</sub>. The analyses above indicate that co-doping of Fe and N may change the functional groups on the biochar surface, which may affect the removal of SMX.

**3.2. Adsorption Kinetics.** The pseudo-first-order (PFO), pseudo-second-order (PSO), Elovich, and intraparticle diffusion models were used to fit the four biochars for SMX adsorption. The optimum parameters for each kinetic model are displayed in Table 3. According to Figure 5a, it can be seen that rapid adsorption occurred within the first 2 h, which indicates that there are enough adsorption sites on the surface of the adsorbent. With time, the active sites of the adsorbent were gradually filled with adsorbent mass. They were reaching the equilibrium stage after around 480 min. Fe-N-BC showed a better SMX removal effectiveness than the other three biochar materials, which was attributed to the higher surface area, sufficient functional groups, and uniform loading of Iron Oxide in Fe-N-BC. The PSO model had higher R<sup>2</sup> values than the PFO model, and this result revealed that the chemisorption involving electron exchange between SMX and the adsorbent was responsible for rate control in the adsorption process. The K<sub>1</sub> value of Fe-N-BC is much higher than N-BC and slightly higher than BC and Fe-BC, which indicates that Fe-N-BC has the highest adsorption rate for SMX.

After fitting with the Elovich model (Figure 5a), the R<sup>2</sup> for both Fe-BC and Fe-N-BC was more than 0.97, further confirming that chemisorption dominates the adsorption process.<sup>47</sup> The rates and steps of the adsorption process were determined by the fitting results from the adsorption kinetic models. The results of the intraparticle diffusion model fit without a straight line past the origin, suggesting that two or three steps control the reaction rate. First, SMX molecules spread rapidly in the outer boundary membrane of biochar. Next, the SMX diffuses at a slower rate inside the biochar pores. Finally, SMX molecules are adsorbed to the inner surface of the biochar, where they slowly approach equilibrium. Therefore, both the outer layer and inner particle diffusion of biochar can be extrapolated to impact the adsorption process.

**3.3. Adsorption Isotherms.** As shown in Figure 5c and Table 4, the adsorption isotherms and fitting parameters of SMX on biochar were obtained. With the increase in equilibrium concentration of the solution, the adsorption amount of SMX on biochars increased and tended to reach equilibrium. The adsorption amount of SMX on biochars increased and tended to reach equilibrium. After being modified with iron and nitrogen, the maximum adsorption capacity of Fe-N-BC for SMX was 42.9 mg/g, which was 1.29 and 1.52 times that of palm fiber biochar (BC) and N-BC, respectively. The Langmuir model had a higher correlation coefficient for fitting N-BC and Fe-N-BC than the Freundlich model, indicating that the adsorption of SMX on these two biochars was dominated by monolayer adsorption, involving chemical and physical adsorption. Furthermore, the separation factor R<sub>L</sub> was between 0 and 1, demonstrating that the adsorption processes of SMX on the two biochars were favorable.<sup>48</sup> Freundlich could better explain the adsorption processes of BC and Fe-BC, indicating that multilayer adsorption was the dominant process that occurred on the heterogeneous surface. The K<sub>F</sub> value can assess the affinity of biochar for contaminants. Among the four biochars, Fe-N-BC had the greatest K<sub>F</sub> value and the highest affinity for SMX. Therefore, Fe-N-BC may have the potential to serve as an effective adsorbent for removing SMX from water.

**3.4. pH Effect.** The charge on the surface of the adsorbent and adsorbate may vary depending on the pH of the solution, thus affecting the adsorption process. As shown in Figure 6b, with the pH increasing from 2 to 11, the adsorption capacity of SMZ on Fe-N-BC rose first then decreased, reaching the maximum of 24.77 mg/L at pH 5, and then fell dramatically to 7.58 mg/L at pH 11. It revealed that the pH of the solution directly influenced SMX adsorption.

The pH of the solution affected the active sites, surface charges, and functional groups on biochar. According to Figure 6a, the points of zero charge (pHpzc) values of N-BC, Fe-BC, and Fe-N-BC were 1.79, 3.97, and 4.837 mV, respectively, demonstrating that the surface potential of biochar increased due to the doping of iron and nitrogen. The pH of the solution can also cause changes in the form of the adsorbate. SMX as an amphoteric compound, the amino group, and the amine sulfonate on the benzene ring can be ionized to exist in different forms at different pH values.<sup>21</sup> SMX in the solution mainly existed as SMX<sup>+</sup> and neutral molecule SMX<sup>0</sup> at the range of pH 3–5. At the same time, there was a part of hydrophobic and hydrophilic groups in the biochar structure, through which SMX<sup>0</sup> was adsorbed by the hydrophobic partition effect and mechanism of dissolution. When pH = 5–7, SMX<sup>0</sup> and SMX<sup>-</sup> existed in two forms, and the adsorption

capacity decreased. At the range of pH 7–11, most of the existing forms of SMX changed to  $\text{SMX}^-$ , and the hydrophobic interaction with biochar was inhibited. At this time, the biochar surface was negatively charged, and there was an electrostatic repulsion with SMX, so the adsorption capacity was further reduced (Figure 6b). Combined with the adsorption capacity at different pH values, we concluded that the adsorption capacity of the three forms of SMX in the adsorbent was in the order of  $\text{SMX}^+ > \text{SMX}^0 > \text{SMX}^-$ .

In addition, Lewis acid–base interaction might occur if the SMX molecule maintained its electrical neutrality.<sup>49</sup> The lone pair carried by the hydroxyl and carboxyl groups on the surface of biochar may interact with the sulfonamide group in SMX. The adsorption affinity of biochar for SMX was enhanced by the Lewis acid–base electronic interaction.

Under the condition of pH 3–5, since the surface of Fe-N-BC was negatively charged, the hydroxyl and carboxyl on the benzene ring could be used as potent  $\pi$ -electron donors. The amino group in the SMX molecule provided lone-pair electrons for the benzene ring; the planar structure of the O-hetero-aromatic rings in the sulfonamide contributed to electronic resonance; therefore, they are used as strong  $\pi$ -electron acceptors with a positive charge. As a result, a stable  $\pi$ - $\pi$  EDA interaction was formed, facilitating the adsorption of SMX on the surface of the biochar.

**3.5. Effect of Coexisting Ion Types and Concentration.** Given the types of substances present in the actual water environment, the impacts of numerous background ions ( $\text{Na}^+$ ,  $\text{Ca}^{2+}$ ,  $\text{NH}_4^+$ , and  $\text{Mg}^{2+}$ ) and ionic strength (0–0.2 mol/L) on the effect of Fe-N-BC for adsorption SMX were examined. According to Figure 6c, with the exception of  $\text{Ca}^{2+}$ , the other ions had little impact on the adsorption action at values below 0.2 mol/L. As the concentration of  $\text{Na}^+$  increased, there was slight improvement in SMX adsorption due to the action of the salting out effect and the squeezing out effect.

However, when the concentration of  $\text{Ca}^{2+}$  in the solution hit 0.2 mol/L, the adsorption capacity fell to 35.2% of the initial amount. This is attributed to the weakly covalent nature of  $\text{Ca}^{2+}$ , allowing for a reduction in the hydration of the high-valent cations, and thus an increase in the interaction between  $\text{Ca}^{2+}$  and the adsorbent surface. As a result,  $\text{Ca}^{2+}$  is more readily adsorbed on biogenic carbon in solution,<sup>29</sup> occupying the adsorption sites of SMX and leading to a decrease in adsorption capacity. As shown in Figure 6d, this study examined the adsorption effect of Fe-N-BC on SMX in synthetic piggery wastewater. Compared with in pure water, the adsorption efficiencies of simulated piggery wastewater, 10-fold, and 50-fold diluted piggery wastewater could be achieved in 82.81, 88.21, and 93.94%, respectively. This implies that other compounds in the wastewater may compete with SMX for pores and active sites on the biochar, preventing SMX from adhering to Fe-N-BC. The fluctuations in adsorption were in the range of 82%, which shows that Fe-N-BC has the ability to resist the interference of ions in the complex water environment and can work steadily in the adsorption process of practical applications.

**3.6. Regeneration Capacity of Biochar.** Following the magnetic separation of Fe-N-BC from SMX solution, four adsorption–desorption cycles using two different sets of regeneration reagents were performed. The results are displayed in Figure 6e,f. After 12 h of treatment with  $\text{H}_2\text{O}_2$  and MeOH, with the increase in cycle times, the adsorption capacity of Fe-N-BC decreased. Compared with the first one,

the last adsorption decreased by 25.47% while the mass loss of biochar reached 19.74%. Under the treatment of MeOH and ammonia, the adsorption capacity was 26.62, 25.81, 25.36, and 25.23 mg/g in the four cycles, respectively, with a cumulative Fe-N-BC loss of 14.8%. This result is explained by the fact that ammonia is not less oxidizing than  $\text{H}_2\text{O}_2$  and has a modest etching effect on biochar, leading to a low loss of biochar mass. Additionally, the pH of the regeneration reagent was adjusted by adding ammonia to methanol, which changed the neutral molecular form of SMZ into the cationic form, facilitating its desorption from Fe-N-BC. Therefore, using a mixture of ammonia and methanol as a regeneration rinse can achieve a stable desorption effect and thus increase the service life of Fe-N-BC.

**3.7. Adsorption Mechanism.** Based on the detection of the adsorption effect, it is indicated that Fe-N-BC has a strong adsorption affinity for SMX, where the adsorption mechanisms involved are pore diffusion, electrostatic interactions, surface complex interactions, hydrogen bonding, Lewis acid–base electron interaction, and  $\pi$ - $\pi$  stacking (Figure 7).<sup>34</sup> The pore

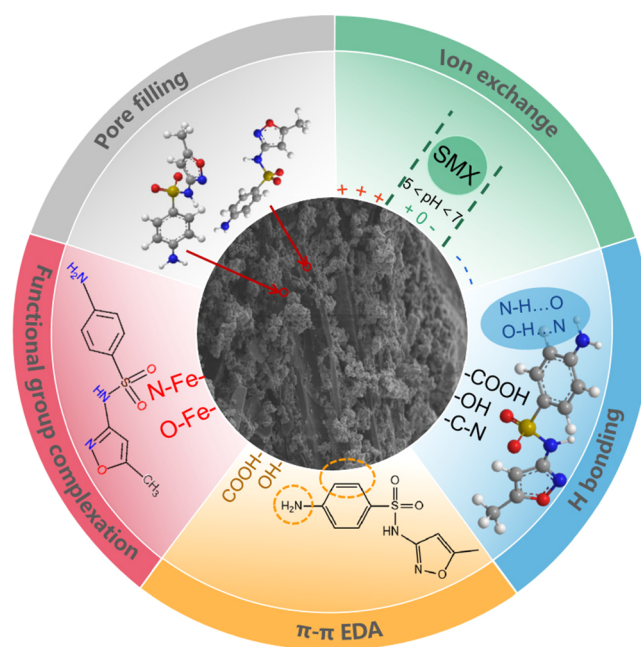


**Figure 7.** Diagrammatic representation of the SMX-to-biochar adsorption process.

size and specific surface area of the biochar played a key role in determining the adsorption effect. After the addition of iron and nitrogen, the adsorption amount of biochar increased along with the surface area and the pore size, while the decrease in the micropore volume unaffected the adsorption effect, proving that the mesopores dominated the pore diffusion mechanism. An abundance of functional groups was found on the biochar surface, which contained oxygen and nitrogen, forming hydrogen bonds with oxygen atoms on the SMX, facilitating the binding of the adsorbent to the SMX. The influence of pH and coexisting cations further revealed that hydrophobic interactions, Lewis acid–base interactions, and  $\pi$ - $\pi$  EDA interactions contribute to adsorption. The hydrophobic interactions between the hydrophobic part of the biochar and the hydrophobic groups on the sulfonamide molecule may increase the adsorption affinity. In addition, the

lone electron pair of the amino group in the aromatic unit of the SMX molecule may form a complex with the surface functional group of the biochar; meanwhile, the benzene ring, amino group, and sulfonamide group on SMX acted as electron acceptors, and the  $\pi$  orbitals of the graphite layer on the biochar acted as donors forming  $\pi$ - $\pi$  bonds.<sup>48</sup> The reduction in the  $I_D/I_G$  value of Fe-N-BC in the Raman spectrum suggests that the adsorption amount of Fe-N-BC on SMX can grow as the degree of graphite carbonization increases. Additionally, it implies that  $\pi$ - $\pi$  stacking is an effective mechanism for this process.

#### 4. CONCLUSIONS

In this work, we prepared a palm fiber biochar modified by co-doping of Fe and N (Fe-N-BC) by the once pyrolysis method, along with BC, N-BC, and Fe-N-BC. Various characterization and adsorption experiments were performed on the biochars. It has been proved that Fe-N-BC exhibits the best adsorption performance due to its significant specific surface area, superior micropore structure, and abundant surface functional groups with a high graphitized degree carbon structure. The adsorption process of SMX on Fe-N-BC followed the PSO kinetic model. In the adsorption process, the rate is impacted by pore filling, surface complexation, hydrogen bonding, and EDA interaction. The results determined that Fe-N-BC is an effective and stable SMX adsorbent. The limitation of this study lies in its environmental applicability, and future studies will focus on the development and practical application of antibiotic removal materials based on the wider environment.

#### ■ ASSOCIATED CONTENT

##### SI Supporting Information

The Supporting Information is available free of charge at <https://pubs.acs.org/doi/10.1021/acsomega.2c06234>.

XPS spectral split peak images of the three biochars (BC, N-BC, Fe-BC) and Raman spectral detail images of the four biochars (PDF)

#### ■ AUTHOR INFORMATION

##### Corresponding Author

**Haoran Yuan** – *School of Municipal & Environmental Engineering, Shandong Jianzhu University, Jinan, Shandong 250000, China; Guangzhou Institute of Energy Conversion, Chinese Academy of Sciences, Guangzhou 510640, China; CAS Key Laboratory of Renewable Energy, Guangdong Provincial Key Laboratory of New and Renewable Energy Research and Development, Guangzhou 510640, China; [orcid.org/0000-0003-1757-4695](https://orcid.org/0000-0003-1757-4695); Email: [yuanhr@ms.giec.ac.cn](mailto:yuanhr@ms.giec.ac.cn)*

##### Authors

**Yuan Diao** – *School of Municipal & Environmental Engineering, Shandong Jianzhu University, Jinan, Shandong 250000, China; Guangzhou Institute of Energy Conversion, Chinese Academy of Sciences, Guangzhou 510640, China; CAS Key Laboratory of Renewable Energy, Guangdong Provincial Key Laboratory of New and Renewable Energy Research and Development, Guangzhou 510640, China*

**Rui Shan** – *Guangzhou Institute of Energy Conversion, Chinese Academy of Sciences, Guangzhou 510640, China; CAS Key Laboratory of Renewable Energy, Guangdong Provincial Key Laboratory of New and Renewable Energy Research and Development, Guangzhou 510640, China; [orcid.org/0000-0002-6181-0061](https://orcid.org/0000-0002-6181-0061)*

**Mei Li** – *School of Municipal & Environmental Engineering, Shandong Jianzhu University, Jinan, Shandong 250000, China*

**Jing Gu** – *Guangzhou Institute of Energy Conversion, Chinese Academy of Sciences, Guangzhou 510640, China; CAS Key Laboratory of Renewable Energy, Guangdong Provincial Key Laboratory of New and Renewable Energy Research and Development, Guangzhou 510640, China; [orcid.org/0000-0002-0291-3263](https://orcid.org/0000-0002-0291-3263)*

**Yong Chen** – *Guangzhou Institute of Energy Conversion, Chinese Academy of Sciences, Guangzhou 510640, China; CAS Key Laboratory of Renewable Energy, Guangdong Provincial Key Laboratory of New and Renewable Energy Research and Development, Guangzhou 510640, China*

Complete contact information is available at:

<https://pubs.acs.org/10.1021/acsomega.2c06234>

#### Notes

The authors declare no competing financial interest.

#### ■ ACKNOWLEDGMENTS

This work was supported by the State's Key Project of Research and Development Plan, China (grant numbers 2020YFC1908900), Science and Technology Program of Guangdong Province, China (grant numbers 2021A1515012263), Science and Technology Program of Guangzhou, China (grant numbers 202002030365), and Guangdong Basic and Applied Basic Research Foundation (grant numbers 2021B1515020068).

#### ■ REFERENCES

- (1) Rana, M. S.; Lee, S. Y.; Kang, H. J.; Hur, S. J. Reducing Veterinary Drug Residues in Animal Products: A Review. *Food Sci. Anim. Resour.* **2019**, *39*, 687–703.
- (2) Zhang, Q. Q.; Ying, G. G.; Pan, C. G.; Liu, Y. S.; Zhao, J. L. Comprehensive evaluation of antibiotics emission and fate in the river basins of China: source analysis, multimedia modeling, and linkage to bacterial resistance. *Environ. Sci. Technol.* **2015**, *49*, 6772–6782.
- (3) Bialk-Bielinska, A.; Stolte, S.; Matzke, M.; Fabianska, A.; Maszkowska, J.; Kolodziejska, M.; Liberek, B.; Stepnowski, P.; Kumirska, J. Hydrolysis of sulphonamides in aqueous solutions. *J. Hazard. Mater.* **2012**, *221–222*, 264–274.
- (4) Chen, J.; Xie, S. Overview of sulfonamide biodegradation and the relevant pathways and microorganisms. *Sci. Total Environ.* **2018**, *640–641*, 1465–1477.
- (5) Baran, W.; Adamek, E.; Ziemianska, J.; Sobczak, A. Effects of the presence of sulfonamides in the environment and their influence on human health. *J. Hazard. Mater.* **2011**, *196*, 1–15.
- (6) Tian, S.; Zhang, C.; Huang, D.; Wang, R.; Zeng, G.; Yan, M.; Xiong, W.; Zhou, C.; Cheng, M.; Xue, W.; Yang, Y.; Wang, W. Recent progress in sustainable technologies for adsorptive and reactive removal of sulfonamides. *Chem. Eng. J.* **2020**, *389*, No. 123423.
- (7) Hu, J.; Li, X.; Liu, F.; Fu, W.; Lin, L.; Li, B. Comparison of chemical and biological degradation of sulfonamides: Solving the mystery of sulfonamide transformation. *J. Hazard. Mater.* **2022**, *424*, No. 127661.
- (8) Xu, H.; Zhu, S.; Zhang, W.; Ji, R. Advances in biodegradation of sulfonamides antibiotics in aerobic activated sludge system. *Chin. J. Biotechnol.* **2021**, *37*, 3459–3474.
- (9) Yu, F.; Li, Y.; Han, S.; Ma, J. Adsorptive removal of antibiotics from aqueous solution using carbon materials. *Chemosphere* **2016**, *153*, 365–385.
- (10) Peiris, C.; Gunatilake, S. R.; Mlsna, T. E.; Mohan, D.; Vithanage, M. Biochar based removal of antibiotic sulfonamides and

tetracyclines in aquatic environments: A critical review. *Bioresour. Technol.* **2017**, *246*, 150–159.

(11) Patel, A. K.; Katiyar, R.; Chen, C. W.; Singhania, R. R.; Awasthi, M. K.; Bhatia, S.; Bhaskar, T.; Dong, C. D. Antibiotic bioremediation by new generation biochar: Recent updates. *Bioresour. Technol.* **2022**, *358*, No. 127384.

(12) Ngigi, A. N.; Ok, Y. S.; Thiele-Bruhn, S. Biochar-mediated sorption of antibiotics in pig manure. *J. Hazard. Mater.* **2019**, *364*, 663–670.

(13) Abd-Elhamid, A. I.; Emran, M.; El-Sadek, M. H.; El-Shanshory, A. A.; Soliman, H. M. A.; Akl, M. A.; Rashad, M. Enhanced removal of cationic dye by eco-friendly activated biochar derived from rice straw. *Appl. Water Sci.* **2020**, *10*, 45.

(14) Xiang, W.; Zhang, X. Y.; Cao, C. C.; Quan, G. X.; Wang, M.; Zimmerman, A. R.; Gao, B. Microwave-assisted pyrolysis derived biochar for volatile organic compounds treatment: Characteristics and adsorption performance. *Bioresour. Technol.* **2022**, *355*, No. 127274.

(15) Goswami, L.; Kushwaha, A.; Kafle, S. R.; Kim, B.-S. Surface Modification of Biochar for Dye Removal from Wastewater. *Catalysts* **2022**, *12*, 817.

(16) Wang, F.; Li, L.; Iqbal, J.; Yang, Z.; Du, Y. Preparation of magnetic chitosan corn straw biochar and its application in adsorption of amaranth dye in aqueous solution. *Int. J. Biol. Macromol.* **2022**, *199*, 234–242.

(17) Shaheen, S. M.; Mosa, A.; Natasha; Abdelrahman, H.; Niazi, N. K.; Antoniadis, V.; Shahid, M.; Song, H.; Kwon, E. E.; Rinklebe, J. Removal of toxic elements from aqueous environments using nano zero-valent iron- and iron oxide-modified biochar: a review. *Biochar* **2022**, *4*, 24.

(18) Zhang, M. D.; He, M. Z.; Chen, Q. P.; Huang, Y. L.; Zhang, C. Y.; Yue, C.; Yang, L. Y.; Mu, J. L. Feasible synthesis of a novel and low-cost seawater-modified biochar and its potential application in phosphate removal/recovery from wastewater. *Sci. Total Environ.* **2022**, *824*, No. 153833.

(19) Feng, Z.; Zhai, X.; Sun, T. Sustainable and efficient removal of paraben, oxytetracycline and metronidazole using magnetic porous biochar composite prepared by one step pyrolysis. *Sep. Purif. Technol.* **2022**, *293*, No. 121120.

(20) Cheng, J.; Hu, S.-C.; Sun, G.-T.; Kang, K.; Zhu, M.-Q.; Geng, Z.-C. Comparison of activated carbons prepared by one-step and two-step chemical activation process based on cotton stalk for supercapacitors application. *Energy* **2021**, *215*, No. 119144.

(21) Shanableh, A.; Bhattacharjee, S.; Alani, S.; Darwish, N.; Abdallah, M.; Mousa, M.; Semreen, M. Assessment of sulfamethoxazole removal by nanoscale zerovalent iron. *Sci. Total Environ.* **2021**, *761*, No. 143307.

(22) Kasera, N.; Kolar, P.; Hall, S. G. Nitrogen-doped biochars as adsorbents for mitigation of heavy metals and organics from water: a review. *Biochar* **2022**, *4*, 17.

(23) Yu, W.; Lian, F.; Cui, G.; Liu, Z. N-doping effectively enhances the adsorption capacity of biochar for heavy metal ions from aqueous solution. *Chemosphere* **2018**, *193*, 8–16.

(24) Li, D.; Chen, W.; Wu, J.; Jia, C. Q.; Jiang, X. The preparation of waste biomass-derived N-doped carbons and their application in acid gas removal: focus on N functional groups. *J. Mater. Chem. A* **2020**, *8*, 24977–24995.

(25) Xu, L.; Wu, C.; Liu, P.; Bai, X.; Du, X.; Jin, P.; Yang, L.; Jin, X.; Shi, X.; Wang, Y. Peroxymonosulfate activation by nitrogen-doped biochar from sawdust for the efficient degradation of organic pollutants. *Chem. Eng. J.* **2020**, *387*, No. 124065.

(26) Kasera, N.; Hall, S.; Kolar, P. Effect of surface modification by nitrogen-containing chemicals on morphology and surface characteristics of N-doped pine bark biochars. *J. Environ. Chem. Eng.* **2021**, *9*, No. 105161.

(27) Liu, G.; Hu, D.; Song, C.; Chen, K.; Du, X.; Chen, D.; Jin, X.; He, F.; Huang, Q. Pyrolysis of different biomass feedstocks impregnated with Mohr's salt to prepare ferrous sulfide-loaded nitrogen-doped biochar composites for sequestration of aqueous Cr(VI) ions. *J. Anal. Appl. Pyrolysis* **2022**, *164*, No. 105545.

(28) Ren, Z.; Wang, Z.; Lv, L.; Ma, P.; Zhang, G.; Li, Y.; Qin, Y.; Wang, P.; Liu, X.; Gao, W. Fe-N complex biochar as a superior partner of sodium sulfide for methyl orange decolorization by combination of adsorption and reduction. *J. Environ. Manage.* **2022**, *316*, No. 115213.

(29) Li, X.; Shi, J.; Luo, X. Enhanced adsorption of rhodamine B from water by Fe-N co-modified biochar: Preparation, performance, mechanism and reusability. *Bioresour. Technol.* **2022**, *343*, No. 126103.

(30) Alhijazi, M.; Zeeshan, Q.; Safaei, B.; Asmael, M.; Qin, Z. Recent Developments in Palm Fibers Composites: A Review. *J. Polym. Environ.* **2020**, *28*, 3029–3054.

(31) Asyraf, M. R. M.; Ishak, M. R.; Syamsir, A.; Nurazzi, N. M.; Sabaruddin, F. A.; Shazleen, S. S.; Norrahim, M. N. F.; Rafidah, M.; Ilyas, R. A.; Abd Rashid, M. Z.; Razman, M. R. Mechanical properties of oil palm fibre-reinforced polymer composites: a review. *J. Mater. Res. Technol.* **2022**, *17*, 33–65.

(32) Acelas, N.; Lopera, S. M.; Porras, J.; Torres-Palma, R. A. Evaluating the Removal of the Antibiotic Cephalexin from Aqueous Solutions Using an Adsorbent Obtained from Palm Oil Fiber. *Molecules* **2021**, *26*, 3340.

(33) Klein, E. Y.; Van Boeckel, T. P.; Martinez, E. M.; Pant, S.; Gandra, S.; Levin, S. A.; Goossens, H.; Laxminarayan, R. Global increase and geographic convergence in antibiotic consumption between 2000 and 2015. *Proc. Natl. Acad. Sci. U. S. A.* **2018**, *115*, E3463–E3470.

(34) Mei, Y.; Xu, J.; Zhang, Y.; Li, B.; Fan, S.; Xu, H. Effect of Fe-N modification on the properties of biochars and their adsorption behavior on tetracycline removal from aqueous solution. *Bioresour. Technol.* **2021**, *325*, No. 124732.

(35) Xu, J.; Zhang, Y.; Li, B.; Fan, S.; Xu, H.; Guan, D.-X. Improved adsorption properties of tetracycline on KOH/KMnO<sub>4</sub> modified biochar derived from wheat straw. *Chemosphere* **2022**, *296*, No. 133981.

(36) Cheng, D.; Ngo, H. H.; Guo, W.; Chang, S. W.; Nguyen, D. D.; Zhang, X.; Varjani, S.; Liu, Y. Feasibility study on a new pomelo peel derived biochar for tetracycline antibiotics removal in swine wastewater. *Sci. Total Environ.* **2020**, *720*, No. 137662.

(37) Penzik, M. V.; Kozlov, A. N.; Zhang, S.; Badenko, V. V.; Sosnovsky, I. K.; Shamansky, V. A. A segmental analysis of pyrolysis of woody biomass. *Thermochim. Acta* **2022**, *711*, No. 179209.

(38) Zago, S.; Bartoli, M.; Muhyuddin, M.; Vanacore, G. M.; Jagdale, P.; Tagliaferro, A.; Santoro, C.; Specchia, S. Engineered biochar derived from pyrolyzed waste tea as a carbon support for Fe-N-C electrocatalysts for the oxygen reduction reaction. *Electrochim. Acta* **2022**, *412*, No. 140128.

(39) Yuliana, M.; Ismadji, S.; Lie, J.; Santoso, S. P.; Soetaredjo, F. E.; Waworuntu, G.; Putro, J. N.; Wijaya, C. J. Low-cost structured alginate-immobilized bentonite beads designed for an effective removal of persistent antibiotics from aqueous solution. *Environ. Res.* **2022**, *207*, No. 112162.

(40) Han, S.; Xiao, P. Catalytic degradation of tetracycline using peroxydisulfate activated by cobalt and iron co-loaded pomelo peel biochar nanocomposite: Characterization, performance and reaction mechanism. *Sep. Purif. Technol.* **2022**, *287*, No. 120533.

(41) Zhong, Q.; Lin, Q.; He, W.; Fu, H.; Huang, Z.; Wang, Y.; Wu, L. Study on the nonradical pathways of nitrogen-doped biochar activating persulfate for tetracycline degradation. *Sep. Purif. Technol.* **2021**, *276*, No. 119354.

(42) Tomczyk, A.; Sokołowska, Z.; Boguta, P. Biochar physicochemical properties: pyrolysis temperature and feedstock kind effects. *Rev. Environ. Sci. Bio/Technol.* **2020**, *19*, 191–215.

(43) Mian, M. M.; Liu, G.; Yousaf, B.; Fu, B.; Ullah, H.; Ali, M. U.; Abbas, Q.; Mujtaba Munir, M. A.; Ruijia, L. Simultaneous functionalization and magnetization of biochar via NH<sub>3</sub> ambient pyrolysis for efficient removal of Cr (VI). *Chemosphere* **2018**, *208*, 712–721.

(44) Li, X.; Jia, Y.; Zhou, M.; Su, X.; Sun, J. High-efficiency degradation of organic pollutants with Fe, N co-doped biochar

catalysts via persulfate activation. *J. Hazard. Mater.* **2020**, *397*, No. 122764.

(45) Qu, S.; Yuan, Y.; Yang, X.; Xu, H.; Mohamed, A. K.; Zhang, J.; Zhao, C.; Liu, L.; Wang, B.; Wang, X.; Rinklebe, J.; Li, Y. C.; Wang, S. Carbon defects in biochar facilitated nitrogen doping: The significant role of pyridinic nitrogen in peroxymonosulfate activation and ciprofloxacin degradation. *Chem. Eng. J.* **2022**, *441*, No. 135864.

(46) Huang, P.; Zhang, P.; Wang, C.; Tang, J.; Sun, H. Enhancement of persulfate activation by Fe-biochar composites: Synergism of Fe and N-doped biochar. *Appl. Catal., B* **2022**, *303*, No. 120926.

(47) Prasannamedha, G.; Kumar, P. S.; Mehala, R.; Sharumitha, T. J.; Surendhar, D. Enhanced adsorptive removal of sulfamethoxazole from water using biochar derived from hydrothermal carbonization of sugarcane bagasse. *J. Hazard. Mater.* **2021**, *407*, No. 124825.

(48) Dai, J.; Meng, X.; Zhang, Y.; Huang, Y. Effects of modification and magnetization of rice straw derived biochar on adsorption of tetracycline from water. *Bioresour. Technol.* **2020**, *311*, No. 123455.

(49) Ahmed, M. B.; Zhou, J. L.; Ngo, H. H.; Guo, W.; Johir, M. A. H.; Sornalingam, K. Single and competitive sorption properties and mechanism of functionalized biochar for removing sulfonamide antibiotics from water. *Chem. Eng. J.* **2017**, *311*, 348–358.